Physical interactions of fish protamine and antisepsis peptide drugs with bacterial membranes revealed by combination of specular x-ray reflectivity and grazing-incidence x-ray fluorescence

Wasim Abuillan,[1] Emanuel Schneck,[2] Alexander Körner,[1] Klaus Brandenburg,[3] Thomas Gutsmann,[3] Tom Gill,[4] Alexei Vorobiev,[5] Oleg Konovalov,[5] and Motomu Tanaka[1,6]

[1]*Physical Chemistry of Biosystems, Institute of Physical Chemistry, University of Heidelberg, D69120 Heidelberg, Germany*

[2]*Institute Laue Langevin, 38042 Grenoble, Cedex 9, France*

[3]*Research Center Borstel, D23845 Borstel, Germany*

[4]*Institute of Fisheries Technology, Dalhousie University, Halifax, Nova Scotia, Canada*

[5]*B3J 2X 4 European Synchrotron Radiation Facility (ESRF), 38053 Grenoble, Cedex 9, France*

[6]*Institute for Integrated Cell-Material Science (WPI iCeMS), Kyoto University, 606-8501 Kyoto, Japan*

(Received 17 January 2013; published 8 July 2013)

As a defined model of outer membranes of gram negative bacteria, we investigated the interaction of monolayers of lipopolysacchrides from *Salmonella enterica* rough strains R90 (LPS Ra) with natural and synthetic peptides. The fine structures perpendicular to the membrane plane and the ion distribution near the interface were determined by specular x-ray reflectivity (XRR) and grazing-incidence x-ray fluorescence (GIXF) in the presence and absence of divalent cations. The unique combination of XRR and GIXF allows for the quantitative identification of different modes of interactions in a high spatial resolution, which cannot be assessed by other experimental methods. Natural fish protamine disrupts the stratified membrane structures in the absence of Ca^{2+} ions, while staying away from the membrane surface in the presence of Ca^{2+} ions. In contrast, synthetic antisepsis peptide Pep 19-2.5 weakly adsorbs to the membrane and stays near the uncharged sugar units even in the absence of Ca^{2+}. In the presence of Ca^{2+}, Pep 19-2.5 can reach the negatively charged inner core without destroying the barrier capability against ions.

DOI: 10.1103/PhysRevE.88.012705 PACS number(s): 87.14.Cc, 87.14.ef, 61.05.cm, 78.70.En

I. INTRODUCTION

The outer surface of gram negative bacteria displays a dense layer of lipopolysaccharides (LPSs) [1] which protects the bacteria against the surroundings. LPSs are also known as endotoxins that induce a strong immune response [2]. A number of *in vivo* studies demonstrated that LPSs prevent the intrusion of cationic antimicrobial peptides (CAPs) into the cell membrane in the presence of divalent ions (Ca^{2+}, Mg^{2+}) [3–5], which has inspired the design of peptide-based antibiotics [6]. Recently, Kowalski *et al.* synthesized a series of 19-mer peptides (P19), and demonstrated that some of them could protect mice against sepsis even at very low concentrations far below the level causing cytotoxicity [7–9].

Previously, Straatsma *et al.* and Kotra *et al.* [10–12] performed molecular dynamics simulations and reported that (i) Ca^{2+} ions are essential for the stability of the LPS membranes [10,12], (ii) most of the Ca^{2+} ions are confined within a thin layer (thickness $\sim$2 nm) in the negatively charged inner core [11], (iii) a well-defined structural pattern existed for the location of the Ca^{2+} ions interacting with the phosphate groups adjacent to inner core saccharides [11,12], and (iv) water penetrated the membrane to a depth of $\sim$3 nm [12]. In order to simulate the conformational changes of molecules on a more realistic time scale ($>10^{-3}$ s) in a large simulation volume containing 100 PAO1 LPS molecules, Pink *et al.* [13] created a "minimum model" of charged wild type LPS strains and carried out a Monte Carlo (MC) simulation of the number density distributions of ions and LPSs including protamine molecules. In our previous accounts, we prepared LPS monolayers at the air-water interface and carried out grazing-incidence x-ray diffraction (GIXD) and grazing-incidence x-ray out of specular plane scattering (GIXOS), where we demonstrated that the observed changes in in-plane and out-of-plane fine structures of LPS monolayers are fully consistent with the MC simulations [14,15]. That is, divalent cations induce a compaction of LPS head groups and increase the chain ordering [14–16]. However, these experiments merely yield the scattering length density profile perpendicular to the membrane plane, but not the density profiles of mono- and divalent ions. In our recent account, we employed x-ray fluorescence (GIXF) to determine the distributions of K^+ and Ca^{2+} ions near LPS Re monolayers [17]. This study revealed that Ca^{2+} ions condense at the negatively charged inner core of LPS Re molecules.

In this paper, we investigate the electrostatics and fine structures of LPS Ra which has a more complex molecular structure close to the wild type LPSs [18]. This molecule consists of six hydrocarbon chains and a carbohydrate head group with inner and outer cores. The inner core consists of two negatively charged phosphorylated glucosamines and two negatively charged 2-keto-3-deoxyoctonoic acid (KDO) units. The outer core has three heptose units (two of them are phosphorylated) and four glucose and *N*-acetylglucosamine units [19]. Here, we prepared monolayers of LPSs at the air-water interface and study the interaction with two types of cationic peptides by the combination of x-ray reflectivity (XRR) and GIXF. As cationic peptides, we used herring protamine used for food preservation and antisepsis peptide (Pep 19-2.5) [19]. Details of the obtained results are presented in the following sections. It should be noted that XRR experiments are essential not only for the structural investigation but also for the GIXF analysis, since the illumination profile significantly depends on the electronic structures of stratified thin layers.

II. MATERIALS AND METHODS

A. Materials and sample preparation

Lipopolysaccharide Ra (LPS Ra) was purified from the bacterial rough strains of *Salmonella enterica* (serovar Minnesota), and the purified sample was lyophilized as reported [20]. The molecules were dissolved in liquid phenol (90%), chloroform, and petroleum ether (2:5:8 by volume). The mixture appeared cloudy and could be made clear by the addition of solid phenol [21]. The stock solution was adjusted to a final concentration of 1 mg/ml. Antisepsis peptide (Pep 19-2.5) was designed as described by Kowalski *et al.* [7,8] and dissolved in phosphate buffered saline (PBS) containing 137 mM NaCl, 2.7 mM KCl, 10 mM $Na_2HPO_4H_2O$, and 1.76 mM KH_2PO_4 at *p*H 7.4 with a concentration of 2.5 mg/ml. Herring protamine (chloride salt) was purified by the method reported in [22] and dissolved in PBS at a concentration of 0.1 g/ml. Unless stated otherwise, chemicals were purchased from Sigma-Aldrich (Munich, Germany) and used without further purification. Double de-ionized water (MilliQ, Molsheim) with a specific resistance of $\rho > 18\ \mathrm{M\Omega\ cm}$ was used throughout this study. The "Ca^{2+}-free" buffer contained 100 mM KCl, 5 mM HEPES. "Ca^{2+}-loaded" buffer additionally contained 50 mM $CaCl_2$. *p*H was adjusted to 7.4 in both cases. LPS Ra monolayers were prepared by spreading LPS Ra solution onto the subphase of a Langmuir film balance. Prior to compression, 20 min was allowed for the complete evaporation of the solvent. The film was compressed to an area per LPS Ra molecule of $A \approx 200\ \text{Å}^2$, which coincides with a surface pressure of $\pi(\text{free}) = 24$ mN/m and $\pi(\text{loaded}) = 10$ mN/m on Ca^{2+}-loaded and Ca^{2+}-free subphases, respectively, as shown in the pressure-area isotherms [19].

B. XRR and GIXF experiments

XRR and GIXF experiments were carried out at the beamline ID10B of the European Synchrotron Radiation Facility (ESRF, Grenoble). The samples were irradiated with a monochromatic synchrotron beam either with an energy of 8 keV ($\lambda = 1.55$ Å) or 10 keV ($\lambda = 1.24$ Å). The film balance was kept in a He atmosphere to minimize the scattering of the fluorescence emission by air and to preserve identical conditions for all measurements. Figure 1 represents a schematic drawing of the experimental setup and scattering geometry for XRR and GIXF experiments.

XRR was measured with a linear detector (Vantec-1, Bruker AXS, USA). After subtraction of the diffuse intensity background (at $\alpha_f \neq \alpha_i$) [19], the specular reflectivity was analyzed using the Parratt formalism [23,24] with a genetic minimization algorithm implemented in the MOTOFIT software package [25].

GIXF measurements were carried out at incident angles α_i below and above the critical angle of total reflection α_c. Here, the penetration depth of the evanescent field depends on the angle of incidence [26–28]:

$$\Lambda(\alpha_i) = \frac{\lambda}{\sqrt{8}\pi}\left[\sqrt{\left(\alpha_i^2 - \alpha_c^2\right)^2 + 4\beta^2} - \left(\alpha_i^2 - \alpha_c^2\right)\right]^{-\frac{1}{2}}, \qquad (1)$$

where β is the imaginary part of the refractive index $n = 1 - \delta + i\beta$.

X-ray fluorescence signals from the chemical elements in the illuminated volume were recorded with an energy sensitive detector (Vortex, SII NanoTechnology, USA) and normalized by the detector counting efficiency. Subsequently, the intensities were normalized by the elastically scattered beam intensity to compensate for systematic differences between the experiments. The incident angle α_i was transformed into the scattering vector component normal to the interface, $q_z = \frac{4\pi}{\lambda}\sin\alpha_i$. In the last step, the fluorescence signals in the presence of monolayers were normalized by the signals from the blank buffer. This procedure avoids artifacts arising from the experimental geometry, such as the size of beam footprint and the fluorescence detector aperture [17].

C. Fluorescence intensities for stratified interfaces

Fluorescence intensity $I_i^f(\alpha)$ from a chemical element i at a distance z from the air-water interface at an incidence angle α can be written as

$$I_i^f(\alpha) = S\int_0^\infty I^{\text{ill}}(z,\alpha)\, c_i(z)\exp(-z/L_i)dz. \qquad (2)$$

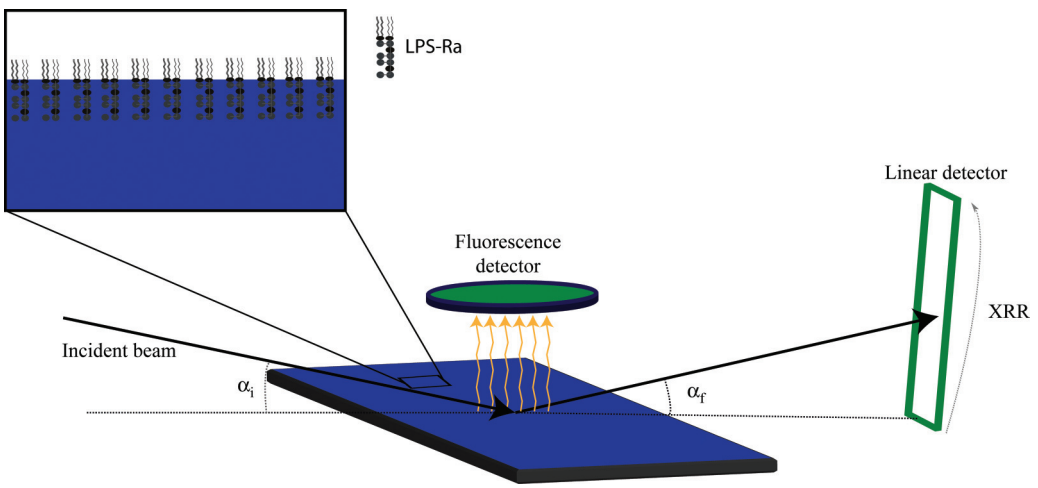

FIG. 1. (Color online) The experimental setup and the scattering geometry used for XRR and GIXF.

S is a proportional constant which is scaled out in our experimental system by the normalization to the fluorescence signal from the corresponding blank buffer, $c_i(z)$ is the concentration of element i at a depth z. The exponential term represents the attenuation of the fluorescence emission between the position z and the detector, where L_i is the attenuation length of water at the characteristic fluorescence line, e.g., $L_{\mathrm{K}-K\alpha} = 68.14\ \mu$m and $L_{\mathrm{Ca}-K\alpha} = 93.7\ \mu$m.

The illumination profile $I^{\mathrm{ill}}(z,\alpha)$ can be determined by the matrix propagation technique [29] using a slabs model. The electron densities and the thicknesses of the slabs are obtained from the XRR analysis. The illumination profile is given by $|E^+(z) + E^-(z)|^2$ where $E^+(z)$ and $E^-(z)$ are the forward and backward propagating waves with respect to the sample surface, respectively. To obtain the exact expression for $E^+(z)$ and $E^-(z)$, the Abelès matrix formalism [30,31] for stratified layers can be split into two parts in layer j in order to determine the electric field amplitudes E_j^+ and E_j^- in layer j:

$$\begin{pmatrix} E_0^+ \\ E_0^- \end{pmatrix} = \frac{C_1 C_2 \cdots C_j}{t_1 t_2 \cdots t_j} \begin{pmatrix} E_j^+ \\ E_j^- \end{pmatrix}, \quad \times \begin{pmatrix} E_j^+ \\ E_j^- \end{pmatrix} = \frac{C_{j+1} C_{j+2} \cdots C_{N+1}}{t_{j+1} t_{j+2} \cdots t_{N+1}} \begin{pmatrix} E_{N+1}^+ \\ 0 \end{pmatrix}, \quad (3)$$

where E_0^+ is the incident wave, E_0^- the reflected wave, E_{N+1}^+ the transmitted wave after layer N, and C_{j+1} is the propagation matrix expressed as

$$C_{j+1} = \begin{bmatrix} \exp(-ik_{zj} \cdot d_j) & r_{j-1} \exp(-ik_{zj} \cdot d_j) \\ r_{j-1} \exp(ik_{zj} \cdot d_j) & \exp(ik_{zj} \cdot d_j) \end{bmatrix}, \quad (4)$$

where k_{zj} is the z component of the wave vector at the interface between layers j and $j+1$, d_j the thickness of layer j, t_j, and r_j are the Fresnel transmission and reflection coefficients, respectively. Since the matrices can be rewritten as

$$C_1 C_2 \cdots C_{N+1} = \begin{pmatrix} a & b \\ c & d \end{pmatrix}, \quad C_{j+1} C_{j+2} \cdots C_{N+1} = \begin{pmatrix} a_j & b_j \\ c_j & d_j \end{pmatrix}, \quad (5)$$

E_j^+ and E_j^- can then be given by the following equations:

$$E_j^+ = t_1 t_2 \cdots t_j \frac{a_j}{a} E_0^+ \quad \text{and} \quad E_j^- = t_1 t_2 \cdots t_j \frac{c_j}{a} E_0^+. \quad (6)$$

Finally, $E^+(z)$ and $E^-(z)$ can be expressed as

$$E^+(z) = E_j^+ \exp\left[ik_{zj}\left(z - \sum_{i=1}^{j-1} d_i\right)\right], \quad E^-(z) = E_j^- \exp\left[-ik_{zj}\left(z - \sum_{i=1}^{j-1} d_i\right)\right]. \quad (7)$$

The concentration profile of the ion species condensed at the carbohydrate head group of LPS Ra was parametrized as [17]

$$c_i(z) = c_0 + c_{\max} \frac{\sqrt{e}(z - z_{\mathrm{HC}})}{z_{\max}} \exp\left[-\frac{(z - z_{\mathrm{HC}})^2}{2z_{\max}^2}\right], \quad (8)$$

where c_0 is the bulk concentration and z_{HC} the position of the interface between hydrocarbon chains and carbohydrate head groups. This enabled us to model ion distributions that possess a concentration maximum with a smooth decay to the bulk concentration with only two free parameters: (i) the concentration maximum $c_{\max}$ and (ii) the z position of this maximum $z_{\max}$. Throughout the GIXF analysis, the Levenberg-Marquardt nonlinear least squares optimization [32] was used for the refinement of the model.

III. RESULTS AND DISCUSSION

A. Impact of Ca^{2+} on the fine structure and electrostatics of LPS Ra

Figure 2(a) shows the XRR curves of LPS Ra monolayers on Ca^{2+}-free (open circles) and Ca^{2+}-loaded (solid circles) together with the best fit results (red lines). For the fitting of the measured XRR curves, the LPS Ra monolayer is modeled with two slabs at the air-water interface: The first slab represents the hydrocarbon chains and the second is for the carbohydrate head group. The layer parameters of LPS Ra previously measured by grazing-incidence x-ray scattering out of specular plane (GIXOS) [15] were used as starting values for the fitting. It should be noted that the monolayer was

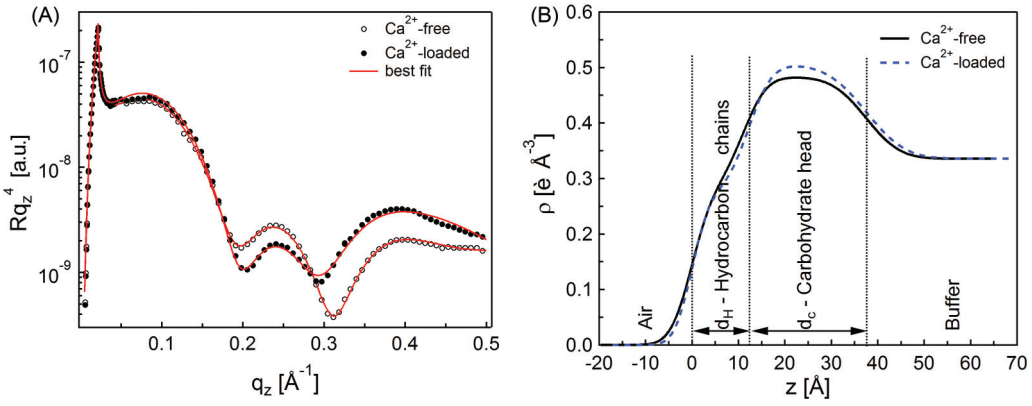

FIG. 2. (Color online) (A) XRR results from LPS Ra monolayer on Ca^{2+}-free buffer (open circles) and Ca^{2+}-loaded buffer (solid circles) together with the best fit results [red (gray) lines]. (B) The reconstructed electron density profiles along the z axis (perpendicular to the interface) for Ca^{2+}-free (black) and Ca^{2+}-loaded (broken blue line) buffers.

TABLE I. Thickness d, electron density ρ, and roughness σ corresponding to best fits of the XRR data of LPS Ra monolayers in the presence and absence of Ca^{2+} [Fig. 2].

LPS Ra on Ca^{2+}-free buffer ($\pi = 24$ mN/m)			
	d (Å)	ρ (e Å^{-3})	σ (Å)
Hydrocarbon chain	11.1 ± 0.3	0.288 ± 0.028	3.7 ± 0.4
Carbohydrate head	26.4 ± 0.7	0.483 ± 0.006	3.9 ± 0.5
Buffer	∞	0.334	5.8 ± 0.1
LPS Ra on Ca^{2+}-loaded buffer ($\pi = 10$ mN/m)			
	d (Å)	ρ (e Å^{-3})	σ (Å)
Hydrocarbon chain	12.2 ± 0.7	0.275 ± 0.029	3.1 ± 0.4
Carbohydrate head	25.4 ± 1.3	0.504 ± 0.007	3.9 ± 0.5
Buffer	∞	0.334	6.7 ± 0.9

prepared from the spreading of LPS Ra dissolved in organic solvents, which enables one to precisely control the spreading amount. This is in contrast to the previous protocol that relied on the spreading of aqueous suspensions [15]. Figure 2(b) represents the reconstructed electron density profiles normal to the monolayer plane, and the layer parameters corresponding to the best fit results are summarized in Table I. These profiles indicate that Ca^{2+} ions induce an increase in the electron density of the carbohydrate head group, accompanied with a slight decrease in the head group thickness. This finding seems consistent with the GIXOS results of Oliveira *et al.* [15], while the improved preparation step seems to result in a more smooth film by avoiding the readsorption of LPS Ra from the bulk subphase. The electron density of the hydrocarbon chains is comparable to previously reported values of phospholipids $\rho \sim 0.3$ e Å^{-3} [33–37].

Figure 3 represents the fluorescence spectra from LPS Ra monolayers on Ca^{2+}-free (top) and Ca^{2+}-loaded (bottom) buffers measured at angles of incidence below ($\alpha_i = 0.1^\circ$, solid squares) and above ($\alpha_i = 0.2^\circ$, open circles) the critical angle of incidence, $\alpha_c = 0.154^\circ$. These spectra were fitted

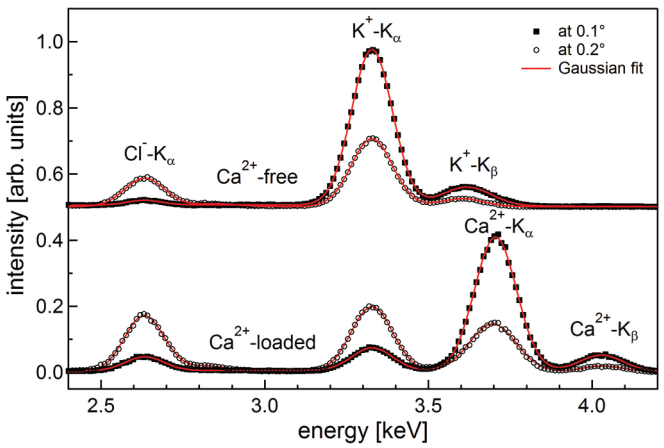

FIG. 3. (Color online) Fluorescence spectra from LPS Ra monolayers on Ca^{2+}-free (top) and Ca^{2+}-loaded buffer (bottom) recorded at angles of incidence below (solid squares) and above (open circles) the critical angle of incidence ($\alpha_i = 0.154^\circ$). The spectra of LPS Ra on Ca^{2+}-free buffer are shifted vertically for clarity. Red (gray) lines indicate the multiple-Gaussian-peaks fitting.

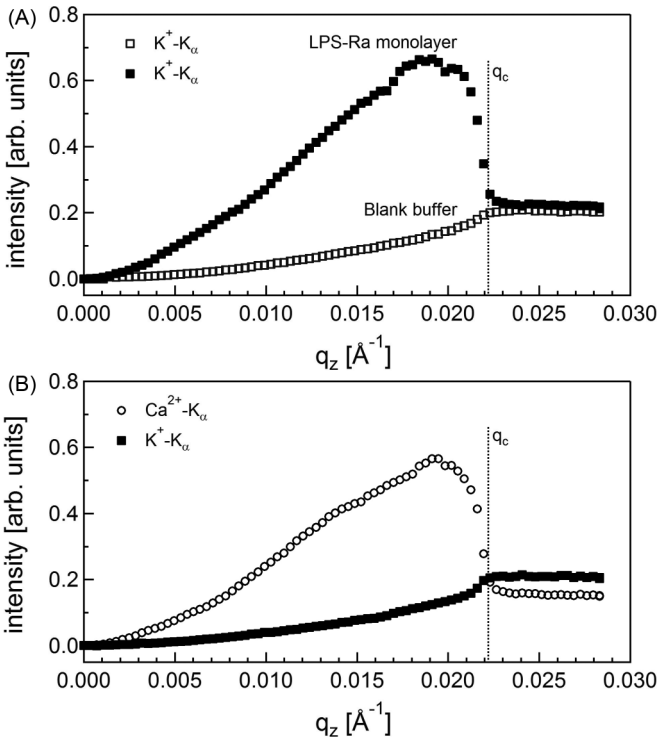

FIG. 4. Fluorescence intensities as a function of q_z, collected on (A) Ca^{2+}-free buffer and (B) Ca^{2+}-loaded buffer. (A) K $K\alpha$ signals in the presence (solid squares) and absence (open squares) of LPS Ra monolayer. (B) Comparison of Ca $K\alpha$ signal (open circles) and K $K\alpha$ signal (solid squares) in the presence of LPS Ra monolayer. The q_z value corresponding to the critical angle (q_c) is indicated by dotted lines.

with a multiple-Gaussian-peaks fitting routine to extract the contribution of each fluorescence characteristic line (Fig. 3, red lines). K $K\alpha$ and K $K\beta$ lines appear at peak positions of 3.31 and 3.59 keV, respectively. Ca $K\alpha$ line has an overlap with K $K\beta$ line at 3.69 keV, while Ca Kβ line has a peak at 4.01 keV. The penetration depth of the evanescent field calculated for $\alpha_i = 0.1^\circ$ and 0.2° can be calculated from Eq. (1), $\Lambda(0.1^\circ) = 60$ Å and $\Lambda(0.2^\circ) = 1309$ Å. In the absence of Ca^{2+} ions (top panel), K $K\alpha$ intensity is enhanced at the interface (solid squares) compared to the signal intensity from the bulk (open circles). On the other hand, Cl^- ions do not show any sign of accumulation to the interface [19]. In the presence of Ca^{2+} ions (bottom panel), Ca $K\alpha$ signal is more pronounced at $\alpha_i = 0.1^\circ$. This finding suggests the condensation of Ca^{2+} ions at the interface, which is in contrast to the K $K\alpha$ signal exhibiting no sign of condensation.

Figure 4 represents the normalized fluorescence signal of each line plotted as a function of q_z. On the Ca^{2+}-free buffer [Fig. 4(a)], the K $K\alpha$ signal below the critical edge ($q_c = 0.022$ Å^{-1}) was much more enhanced in the presence of a LPS Ra monolayer (solid squares) than that on the blank buffer (open squares). This finding implies the enrichment of K^+ ions near the air-water interface through interaction with the LPS Ra surface. On the Ca^{2+}-loaded buffer [Fig. 4(b)], the K $K\alpha$ signal in the presence of a LPS Ra monolayer (solid squares) is comparable to the signal on the blank buffer. In contrast, the Ca $K\alpha$ signal (open circles) exhibited a prominent

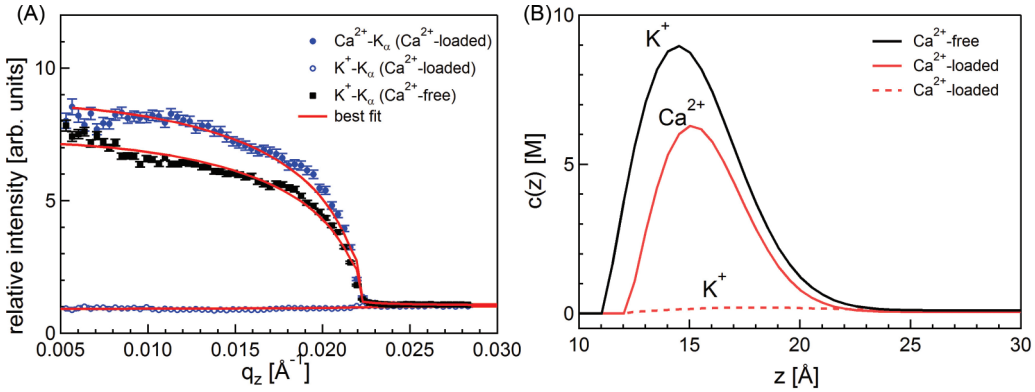

FIG. 5. (Color online) (A) Normalized fluorescence intensities from LPS Ra monolayers as a function of q_z of K $K\alpha$ (black solid squares) on Ca^{2+}-free buffer, K $K\alpha$ (blue open circles), and Ca $K\alpha$ (blue solid circles) on Ca^{2+}-loaded buffer. Vertical bars are $\pm$ standard deviation obtained from Gaussian error propagation during the fit of the fluorescence spectra. The red (gray) lines indicate the best fit from Eq. (2) to the experimental data. (B) The corresponding ion concentration profiles normal to the interface obtained from the fits for K^+ ions (black line) on Ca^{2+}-free buffer, K^+ ions (broken line), and Ca^{2+} ions [red (gray) line] on Ca^{2+}-loaded buffer.

peak at $q<q_c$, indicating the condensation of Ca^{2+} ions near the interface. The depletion of K^+ ions and condensation of Ca^{2+} observed on Ca^{2+}-loaded buffer suggests that K^+ ions near the interface are replaced by Ca^{2+} ions. It should be noted that the measured fluorescence signals are given as a function of illumination intensity, concentration profile normal to the interface, the quantum yield of each element, and the reabsorption from the bulk medium (water). Therefore, we normalize the fluorescence signals by the corresponding signals from the blank buffer and exclude the artifacts from different lines and geometrical effects. In addition, the $K\alpha$ lines were used to reconstruct the concentration profiles since they are more intense than the $K\beta$ lines (Fig. 3) [19].

The black solid squares in Fig. 5(a) represent the normalized K $K\alpha$ signals from LPS Ra monolayer on the Ca^{2+}-free buffer (solid squares) given as a function of q_z. The blue open and solid squares in panel (A) are K $K\alpha$ and Ca $K\alpha$ from the LPS Ra monolayer on the Ca^{2+}-loaded buffer, respectively. The experimental data were fitted by Eq. (2) as $I_{\text{relative}} = I_{\text{normalized-LPS}}/I_{\text{normalized-buffer}}$. Here, the illumination intensity was calculated using the values obtained from the XRR analysis (Table I). The concentration profile of the ion species condensed near the interface was modeled using Eq. (8), taking bulk concentrations of $c_0 = 0.1$ M and $c_0 = 0.05$ M for K^+ and Ca^{2+}, respectively. On the other hand, we assumed constant ion concentration profiles for blank buffers, since the ion depletion near the interface is negligibly small in the absence of surfactant films [38]. The value of z_{HC} in Eq. (8) is provided from the thickness of hydrocarbon chains obtained by XRR; $d = 11.1$ and 12.2 Å in the absence and presence of Ca^{2+}, respectively. The ion concentration profiles corresponding to the best fit results in Fig. 5(a) are presented in Fig. 5(b). The distribution of K^+ ions on the Ca^{2+}-free buffer (black solid line) has a clear peak at $z_{\max} = 15$ Å, $c_{\max} = 8.6 \pm 0.5$ M. The peak position ($z_{\max} = 15$ Å) corresponds to the inner core saccharides of a LPS Ra molecule, possessing four negatively charged saccharide units (two phosphorylated glucosamine units and two KDO units). Integrating the excess ion concentration along the z axis yields the lateral density of K^+ ions, $c_L = (2.9 \pm 0.25) \times 10^{14}$ ions/cm^2. Taking the area occupied by one LPS Ra molecule on Ca^{2+}-free buffer ($A = 200$ Å^2), one can quantitatively determine the number of K^+ ions bound to one LPS Ra molecule, $N = 5.9 \pm 0.6$. This can be understood from the conservation of charge neutrality, since one LPS Ra can carry negative charges up to $Q_{\text{LPS-Ra}} \sim -6\,e$.

The red lines in Fig. 5(b) represent the concentration profiles of Ca^{2+} (solid) and K^+ (broken) ions on Ca^{2+}-loaded buffer. First, it should be noted that the concentration of K^+ ions near the interface is almost identical to the bulk concentration, while Ca^{2+} ions exhibit a distinct maximum at $z_{\max} = 16$ Å, corresponding to the concentration of $c_{\max} = 6.2 \pm 0.3$ M. Integrating the excess concentration along the z axis yields the lateral density of Ca^{2+} ions $c_L = (1.8 \pm 0.1) \times 10^{14}$ ions/cm^2. If one takes the area per molecule on Ca^{2+}-loaded buffer ($A = 192$ Å^2), we can quantify that $N = 3.5 \pm 0.3$ Ca^{2+} ions are associated with one LPS Ra molecule. Note that the chloride ions are neglected in the calculation of the total effective charge of LPS Ra molecules [19].

It should also be noted that the normalized K^+ fluorescence intensity in Ca^{2+}-loaded buffer [Fig. 5(a), blue open circles] at $q_z<q_c$ is slightly less than unity. Though this may be attributed to the depletion of K^+ ions near the interface, the corresponding concentration profile [Fig. 5(b), red broken line] obtained from the fit indicates that the K^+ ion concentration at the head group region is slightly higher than the bulk concentration. In fact, the estimated number of K^+ ions associated with the LPS Ra molecule is $N = 0.3 \pm 0.2$. We concluded that the slightly lower intensity at $q<q_c$ reflects the modification of the electron density at the air-water interface in the presence of the LPS Ra monolayer.

The observed replacement of monovalent cations by divalent cations from the negatively charged inner core saccharides is consistent with our previous study of LPS Re possessing only inner core saccharide units [18]. Compared to the simulation we used previously, the fitting of $c_{\max}$ and $z_{\max}$ developed in this study allows for the localization of ions with a higher precision ($z_{\max} \pm 3$ Å) [19], unraveling the condensation of ions in the charged inner core saccharides of a more complex LPS Ra molecule. Our experimental results are in a good

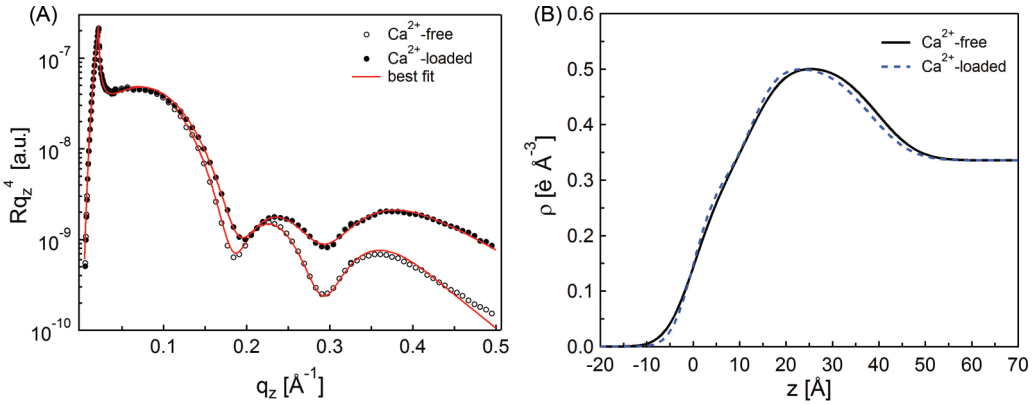

FIG. 6. (Color online) (A) XRR results from LPS Ra monolayer on Ca^{2+}-free buffer (open circles) and Ca^{2+}-loaded buffer (solid circles) after the injection of Pep 19-2.5 underneath LPS Ra monolayers. The best fits to the experimental results are presented as red (gray) lines. (B) The electron density profiles reconstructed from the best fits.

agreement with the number density of K^+ and Ca^{2+} ions calculated from the coarse-grained Monte Carlo simulations on LPS Ra [15] as well as the molecular dynamic simulations [10–12].

Moreover, the presented ions' distributions exhibit peaks at around $z_{max}\sim$15 Å which decay gradually and reach the bulk concentration near $z\sim$22 Å. Since the total thickness of the LPS Ra monolayer in the absence or presence of Ca^{2+} is around $d = 37.5$ Å, the fast decay in ion density profiles suggests that the majority of ions are accumulated near the KDO and phosphorylated saccharide units but not around the uncharged saccharide units in the outer core.

B. Interaction of Pep 19-2.5 with LPS Ra monolayer

The interactions of antisepsis peptide Pep 19-2.5 with LPS Ra monolayers in the absence and presence of Ca^{2+} were studied by injecting Pep 19-2.5 into the subphase underneath LPS Ra monolayers to reach the final bulk concentration of 7 μg/ml. On Ca^{2+}-free buffer, the surface pressure (π = 24 mN/m) increased up to $\pi\approx$50 mN/m. On the other hand, although the initial surface pressure was much lower (π = 10 mN/m), the LPS monolayer on Ca^{2+}-loaded buffer showed an increase of the surface pressure to $\pi = 27$ mN/m.

Figure 6(a) shows the XRR curves of LPS Ra after the injection of Pep 19-2.5 in the absence (open circles) and the presence (solid circles) of Ca^{2+}. The best fits matching to the results are shown in red lines. To evaluate the change in the monolayer structure caused by Pep 19-2.5, the parameters of the LPS Ra monolayers obtained from the fits prior to the peptide injection (Table I) were used as the starting values for fitting.

In the absence of Ca^{2+}, the injection of Pep 19-2.5 led to an increase in the electron density of the head groups from ρ = 0.483 e Å^{-3} to 0.506 e Å^{-3}, accompanied with a small increase in the total monolayer thickness ($\delta d = 0.7$ Å). Moreover, we also observed an increase in the roughness of each layer. The observed increase in the electron density, thickness, and roughness seems consistent with a significant increase in the surface pressure to $\pi = 50$ mN/m. These results suggest that Pep 19-2.5 molecules do not only adsorb on the monolayer surface but also go deeper into the head group region of the LPS Ra monolayer in the absence of Ca^{2+} ions. It is noteworthy that the electron density profile of the LPS Ra monolayer can

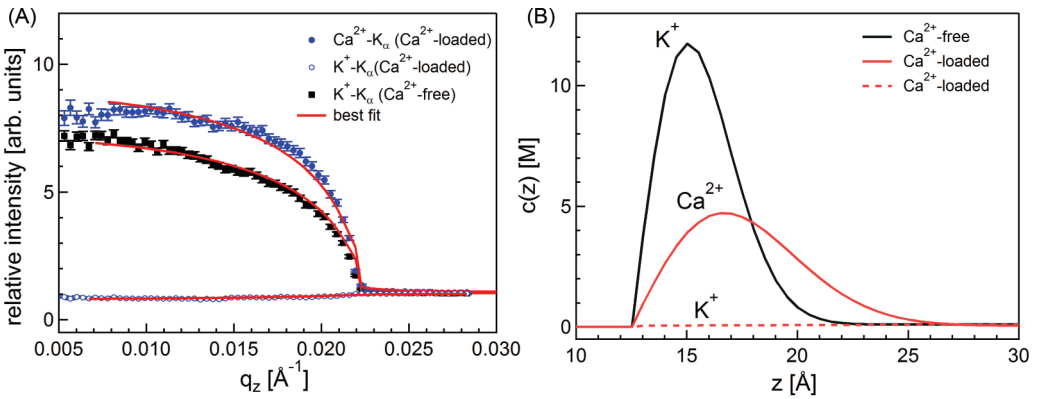

FIG. 7. (Color online) (A) Normalized fluorescence intensities from LPS Ra monolayers with Pep 19-2.5 as a function of q_z of K $K\alpha$ (black solid squares) on Ca^{2+}-free buffer, K $K\alpha$ (blue open circles), and Ca $K\alpha$ (blue solid circles) on Ca^{2+}-loaded buffer. Vertical bars are $\pm$ standard deviation obtained from Gaussian fitting of the fluorescence spectra. The red (gray) lines indicate the best fit from Eq. (2) to the experimental data. (B) The corresponding ion concentration profile normal to the interface obtained from the fits for K^+ ions (black line) on Ca^{2+}-free buffer, K^+ ions (broken line), and Ca^{2+} ions [red (gray) line] on Ca^{2+}-loaded buffer.

TABLE II. Thickness d, electron density ρ, and roughness σ corresponding to the best fits of the XRR of LPS Ra after the injection of Pep 19-2.5 solution into the subphase [Fig. 6].

LPS Ra + Pep 19-2.5 on Ca^{2+}-free buffer ($\pi = 50$ mN/m)			
	d (Å)	ρ (e Å^{-3})	σ (Å)
Hydrocarbon chain	12.5 ± 0.7	0.280 ± 0.008	4.8 ± 0.6
Carbohydrate head	27.1 ± 1.2	0.506 ± 0.008	5.6 ± 0.4
Buffer	∞	0.334	6.9 ± 0.1
LPS Ra + Pep 19-2.5 on Ca^{2+}-loaded buffer ($\pi = 27$ mN/m)			
	d (Å)	ρ (e Å^{-3})	σ (Å)
Hydrocarbon chain	12.5 ± 0.6	0.293 ± 0.015	3.8 ± 0.4
Carbohydrate head	25.5 ± 1.4	0.504 ± 0.007	4.4 ± 0.6
Buffer	∞	0.334	7 ± 0.6

still be represented by stratified "slabs" even in the absence of Ca^{2+}. This is in contrast to our previous studies on herring protamine, where we observed the destruction of the layered structures caused by the protamine injection [18].

On the other hand, in the presence of Ca^{2+}, the increase in surface pressure was not accompanied with the destruction of monolayer structures. The thickness and the electron density of both the hydrocarbon chains and the carbohydrate head groups remained almost identical before and after the injection of Pep 19-2.5, but, similar to the case of Ca^{2+}-free buffer, we observed an increase in the roughness of each layer [19]. The increase in the surface pressure and the interfacial roughness implies that Pep 19-2.5 molecules weakly interact with the LPS Ra monolayer without destroying the stratified layer structures. In fact, there was no improvement in the quality of the reflectivity analysis by using additional slab assuming another Pep 19-2.5 layer.

The black solid squares in Fig. 7(a) represent the normalized fluorescence intensities of K $K\alpha$ from LPS Ra monolayer on Ca^{2+}-free buffer after Pep 19-2.5 injection. The K $K\alpha$ and Ca $K\alpha$ signals from the same monolayer on Ca^{2+}-loaded buffer are indicated by blue open and solid circles, respectively. The best fit results of the GIXF signals are shown as red lines in Fig. 7(a).

The concentration profile of K^+ on Ca^{2+}-free buffer reconstructed from the best fit result [red line, Fig. 7(a)] is presented as a black line in Fig. 7(b). It should be noted that the peak position of K^+ distribution ($z_{max} = 15$ Å) was found at the same position as the one in the absence of Pep 19-2.5 (Fig. 10(a)). In addition, the K^+ concentration decays to the bulk level at $z = 22$ Å and $z = 23$ Å in the absence and presence of Pep 19-2.5, respectively. These changes are below the z resolution (±3 Å) of GIXF. In fact, the number of K^+ ions associated with one LPS Ra molecule ($N = 5.8 \pm 0.6$) is almost equal to that in the absence of Pep 19-2.5 ($N = 5.9 \pm 0.6$). These results thus demonstrated that the distribution of K^+ ions in the negatively charged inner core saccharide region remains intact even in the presence of Pep 19-2.5 molecules. This observation suggests that the Pep 19-2.5 molecules adsorb into the peripheral part of the LPS Ra monolayer, but do not reach the charged inner core region. This interpretation is further supported by the intactness of the electron density and the thickness of the hydrocarbon chain region (Tables I and II).

The red lines in Fig. 7(b) represent the density profiles of Ca^{2+} (solid) and K^+ (broken) ions on Ca^{2+}-loaded buffer after Pep 19-2.5 injection. Similar to the results obtained in the absence of Pep 19-2.5 [Fig. 5(b)], we observed the replacement of K^+ ions by Ca^{2+} ions. However, in contrast to the K^+ distribution on Ca^{2+}-free buffer, the density profile of Ca^{2+} ions has a peak at $z_{max} = 17$ Å [Fig. 10(b)], which is shifted from the position before injecting Pep 19-2.5 ($z_{max} = 15$ Å). Moreover, a clear broadening of the Ca^{2+} distribution could be observed. Here, the Ca^{2+} concentration reaches the bulk level at $z = 26$ Å. On the other hand, the numbers of Ca^{2+} and K^+ ions associated with one LPS Ra molecule are almost identical to those in the absence of Pep 19-2.5, $N_K = 0.5 \pm 0.1$, and $N_{Ca} = 3.7 \pm 0.3$, respectively. However, the broadening of the Ca^{2+} distribution as well as the increase in the surface pressure to 27 mN/m do not cause any remarkable change in the thickness, electron density, and roughness of the head group region, suggesting that the adsorption of Pep 19-2.5 on Ca^{2+}-loaded buffer is much weaker than that on Ca^{2+}-free buffer.

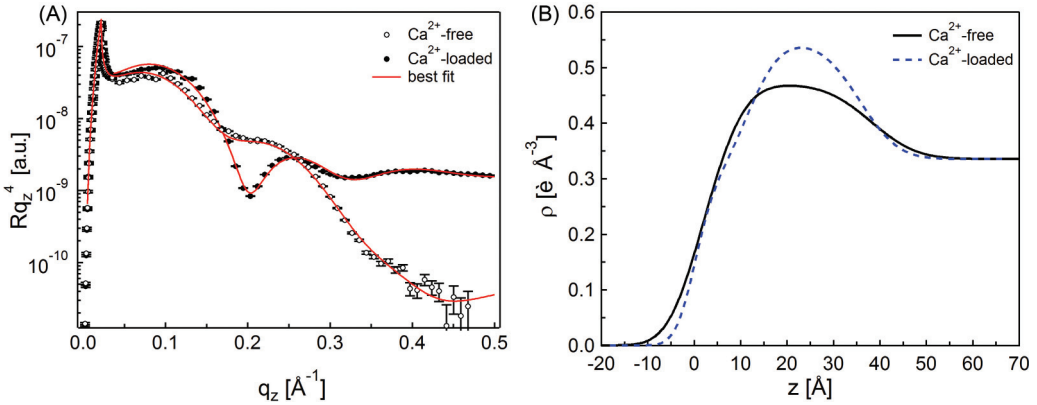

FIG. 8. (Color online) (A) XRR results from LPS Ra monolayer on Ca^{2+}-free buffer (open circles) and Ca^{2+}-loaded buffer (solid circles) after the injection of protamine underneath LPS Ra monolayer together with the best fits [red (gray) lines] matching the experimental results. (B) Indicated the reconstructed electron density profile perpendicular to the interface.

TABLE III. Thickness d, electron density ρ, and roughness σ corresponding to best fits of the XRR of LPS Ra after protamine injection into the subphase [Fig. 7].

LPS Ra + protamine on Ca^{2+}-free buffer ($\pi = 50$ mN/m)			
	d (Å)	ρ (e Å^{-3})	σ (Å)
Hydrocarbon chain	7.1 ± 2.3	0.299 ± 0.015	5.3 ± 0.9
Carbohydrate head	31.1 ± 5.1	0.470 ± 0.073	5.3 ± 3.7
Buffer	∞	0.334	7.7 ± 4.1
LPS Ra + protamine on Ca^{2+}-loaded buffer ($\pi = 24$ mN/m)			
	d (Å)	ρ (e Å^{-3})	σ (Å)
Hydrocarbon chain	11.3 ± 0.1	0.276 ± 0.007	3.3 ± 0.1
Carbohydrate head	24.4 ± 0.2	0.546 ± 0.009	5.6 ± 0.3
Buffer	∞	0.334	6.6 ± 0.2

The fact that the injection of Pep 19-2.5 causes almost no change in the K^+ distribution on Ca^{2+}-free buffer [black lines in Figs. 5(b) and 7(b)] suggests that the slight increase in the electron density ($\Delta\rho_m = 0.023\ e$ Å^{-3}) and the thickness ($\Delta d_C = 0.7$ Å) of the head group region is caused by the penetration of Pep 19-2.5 molecules into the saccharide head group up to z>22 Å. Here, the volume fraction of Pep 19-2.5 within the head group layer φ_{P19} can be obtained by $\varphi_{P19} = \frac{\Delta\rho_m}{\rho_{dry}-\rho_{buffer}}$ where ρ_{dry} and ρ_{buffer} are the electron densities of Pep 19-2.5 in the dry state and in the blank buffer, respectively. From the known amino acid sequence of Pep 19-2.5 [8], one can estimate the molecular volume of Pep 19-2.5 to be $V_{P19} = 3346 \pm 24$ Å^3 [39,40] and its electron density in the dry state to be $\rho_{dry} = 0.433 \pm 0.003\ e$ Å^{-3}, yielding $\varphi_{P19} = 23\%$. Taking the area per molecule on Ca^{2+}-free buffer ($A = 200$ Å^2) and the thickness of the head group region ($d_C = 27.1$ Å), the number of Pep 19-2.5 molecules interacting with one LPS Ra molecule can be calculated to be $N = 0.37$. This value seems to be in excellent agreement with the number of Pep 19-2.5 per one LPS Ra molecule, estimated from the isothermal titration calorimetry experiments $N = 0.3$ [8,9,41].

C. Interaction of fish protamine with LPS Ra monolayer

Protamine is a naturally occurring cationic antibacterial peptide (CAP) used in the food industry as a food preservative. To determine the influence of protamine on the electrostatics and the structure of the LPS Ra monolayer, herring protamine was injected into the subphase to a final concentration of 1 mg/ml, which is comparable with the minimum inhibitory concentration determined by *in vivo* experiments (1.25 mg/ml) [42]. On Ca^{2+}-free buffer, the injection of protamine led to an abrupt increase in the surface pressure of LPS Ra monolayers up to $\pi = 50$ mN/m, which is close to the value we reported previously (45 mN/m) [15]. On the other hand, a LPS Ra monolayer on Ca^{2+}- loaded buffer remained almost intact, showing a very small increase in the surface pressure ($\Delta\pi < 5$ mN/m).

Figure 8(a) shows the XRR data of LPS Ra monolayers after protamine injection on Ca^{2+}-free (open circles) and Ca^{2+}-loaded (solid circles) buffers with the best matching fits (red lines). The parameters obtained from the best fitting results are summarized in Table III. The electron density profiles reconstructed from the fits are presented in Fig. 8(b), where the black line stands for the calcium-free subphase and the blue broken line for the calcium-loaded subphase.

In the absence of Ca^{2+}, we observed a drastic decrease in the hydrocarbon chain's layer thickness down to $d_H = 7.1$ Å and a clear increase in the head group layer thickness ($d_C = 31.1$ Å). Moreover, the roughness of all interfaces showed a clear increase compared to the corresponding values presented in Table I. In addition, the modifications of the electron density profile [Figs. 2(b) and 8(b)] and a significant increase in the surface pressure ($\Delta\pi \sim 30$ mN/m) suggest that the protamine molecules disrupt the overall structure of the LPS Ra monolayer. This makes it difficult to distinguish chains and head groups as independent slabs. In contrast, in the presence of Ca^{2+}, the structure of the LPS Ra monolayer is almost retained even after the protamine injection. The slight differences in the electron density of head groups can be attributed to the deviation in the lateral compression caused by different preparations.

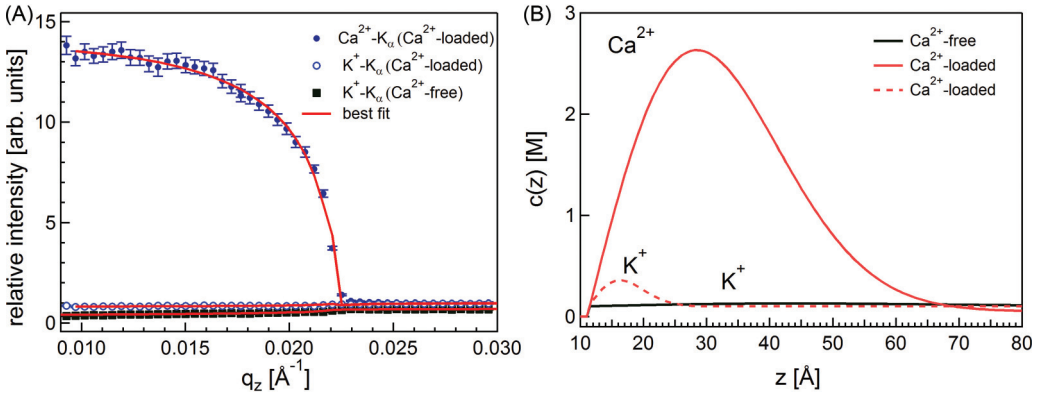

FIG. 9. (Color online) (A) Normalized fluorescence intensities from LPS Ra monolayers with protamine as a function of q_z of K $K\alpha$ (black solid squares) on Ca^{2+}-free buffer, K $K\alpha$ (blue open circles), and Ca $K\alpha$ (blue solid circles) on Ca^{2+}-loaded buffer. Vertical bars are ± standard deviation obtained from Gaussian fitting of the fluorescence spectra. The red lines indicate the best fit from Eq. (2) to the experimental data. The K $K\alpha$ curve on Ca^{2+}-free buffer is shifted with an offset of −0.3 to discriminate it from the one on Ca^{2+}-loaded buffer (B) The corresponding ion concentration profile normal to the interface obtained from the fits for K^+ ions (black line) on Ca^{2+}-free buffer, K^+ ions (broken line), and Ca^{2+} ions [red (gray) line] on Ca^{2+}-loaded buffer.

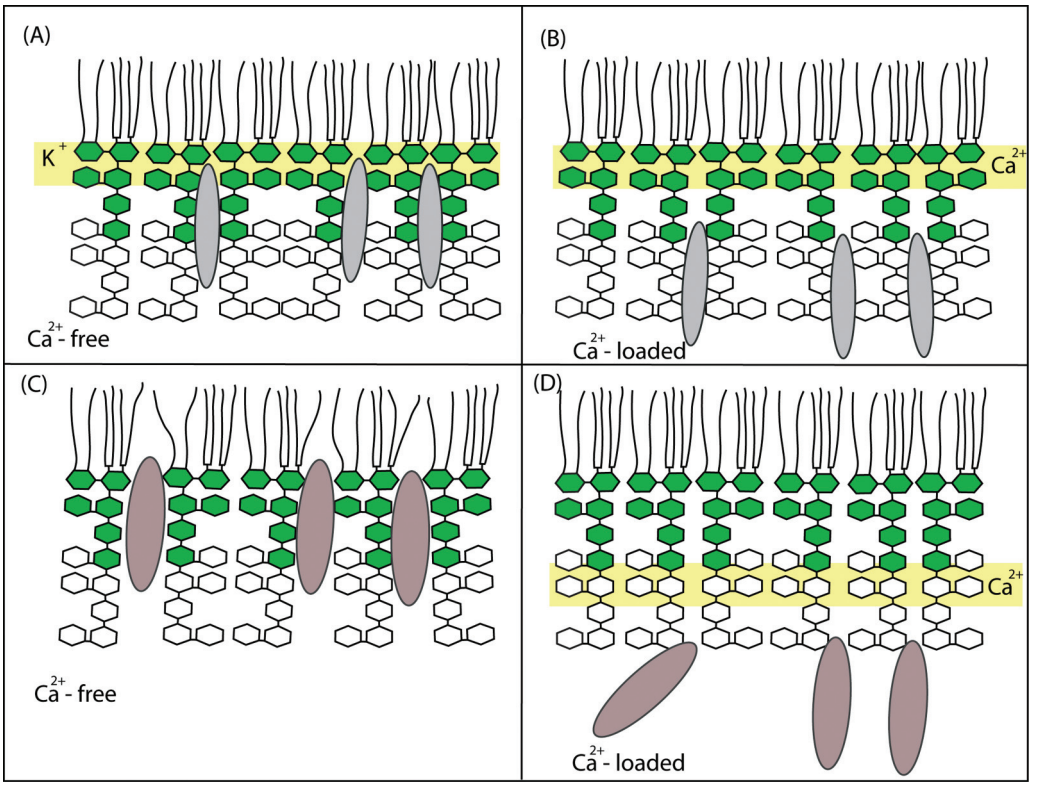

FIG. 10. (Color online) Illustration showing the suggested interaction mechanisms of LPS Ra monolayers with Pep 19-2.5 indicated in gray ellipses (A) and (B) and with protamine indicated in brown (medium gray) ellipses (C) and (D) on Ca^{2+}-free buffer (left panel) and on Ca^{2+}-loaded buffer (right panel). The yellow (light gray) area indicates the position of the maximum concentration.

In Fig. 9(a), the normalized K $K\alpha$ fluorescence intensities of LPS Ra monolayers in the presence of protamine on Ca^{2+}-free buffer are presented by solid black squares, and the signals from K $K\alpha$ and Ca $K\alpha$ on Ca^{2+}-loaded buffer are in blue open and solid circles. The best fit results are labeled with red lines in the same panel. It is remarkable that the concentration profile of K^+ ions [black line, Fig. 9(b)] has a constant value equal to the bulk concentration ($c_0 = 0.1$ M) up to the air-water interface, which is completely different from that in the case of P19-2.5. This means that protamine molecules fully replace the K^+ ions in the charged inner core saccharides and completely compensate the negative charge of the LPS Ra molecule despite the presence of 100 mM salt. This demonstrates that LPS Ra monolayer cannot act as a nonpermeable barrier against protamine molecules when only monovalent K^+ ions are present [Fig. 10(c)].

On Ca^{2+}-loaded buffer, K^+ ions are mostly displaced from the head group region and the concentration profile [red broken line in Fig. 9(b)]. The amount of K^+ ions remaining was below the detection limit ($N = 0.2 \pm 0.6$). The maximum Ca^{2+} concentration is located at $z_{max} = 30$ [Fig. 10(d)], yielding the calculated number of Ca^{2+} ions associated with one LPS Ra molecule which is $N = 7.3 \pm 0.5$ [solid red line in Fig. 9(b)]. This is almost double the number of Ca^{2+} ions associated with one LPS Ra molecule in the presence of Pep 19-2.5, which cannot be attributed to the compensation of negative charges in core saccharide units. In fact, the concentration of Ca^{2+} does not decay to the bulk level until it reaches $z = 70$ Å, which is far beyond the thickness of saccharide head groups ($z =$ 36 Å). Ca^{2+} ions tend to accumulate near the head group–water interface in the presence of protamine, which carries a large amount of positive charges ($Q \sim +20\ e$). This can be rather interpreted within the framework of dielectric continuum theory [43–45] which explains the accumulation of large, strongly polarizable ions as the gain in the cavitational energy with a small electrostatic energy penalty. The authors also calculated the density profiles of trivalent ions, monovalent ions, and anions around a negatively charged colloidal particle and showed that the anions are pushed away from the colloidal surface [45,46]. A similar tendency was also observed, though in a less pronounced manner, for Pep 19-2.5 carrying less positive charge ($Q = +7.7\ e$) and two orders of magnitude lower in concentration.

IV. CONCLUSIONS

We combine x-ray reflectivity (XRR) and grazing-incidence x-ray fluorescence (GIXF) at the air-water interface to determine quantitatively the vertical fine structures and the ion distributions on the model of bacterial membrane surfaces. By systematic studies on antisepsis peptide drug (P19-2.5) and fish protamine, it has been demonstrated that the unique combination of XRR and GIXF is a powerful tool to identify different modes of interactions between complex and realistic biomembrane models and membrane-active molecules. In the absence of divalent ions, Pep 19-2.5 reaches charged inner core saccharides without destroying the barrier capability against ions, while protamine penetrates across the membrane and

reaches the air-water interface that results in the structural integrity of the membrane. In the presence of divalent ions, Pep 19-2.5 weakly adsorbs to the membrane and stays near the uncharged sugar units, while protamine is further pushed away from the head group. Moreover, a clear difference in the number of Ca^{2+} ions associated with one LPS Ra molecule ($N = 7.3$ for protamine, $N = 3.7$ for Pep 19-2.5, and $N = 3.5$ in their absence) cannot be explained by the compensation of negative charges in core saccharide units. Our finding may be interpreted within the framework of dielectric continuum theory that explains the accumulation of large, strongly polarizable ions.

ACKNOWLEDGMENTS

We thank ESRF for synchrotron beam time and German Science Foundation (Grant No. GRK 1114) for support. W.A. thanks GRK for support through a doctoral fellowship, and E.S. is supported by Marie Curie fellowship. W.A., E.S., and M.T. thank D. A. Pink for stimulating discussion. M.T. is a member of the German Excellence Initiative "CellNetwork" and the Helmholtz Program "BioInterface." The iCeMS is supported by World Premier International Research Center Initiative (WPI), MEXT, Japan.

[1] O. Lüderitz, M. A. Freudenberg, C. Galanos, V. Lehmann, E. T. Rietschel, D. H. Shaw, B. Felix, and K. Arnost, in *Current Topics in Membranes and Transport* (Academic Press, New York, 1982), p. 79.

[2] C. Alexander and E. T. Rietschel, J. Endotoxin Res. **7**, 167 (2001).

[3] T. D. Brock, Can. J. Microbiol. **4**, 65 (1958).

[4] L. T. Hansen, J. W. Austin, and T. A. Gill, Int. J. Food Microbiol. **66**, 149 (2001).

[5] N. M. Islam, T. Itakura, and T. Motohiro, Nippon Suisan Gakkaishi **50**, 1705 (1984).

[6] R. E. W. Hancock and D. S. Chapple, Antimicrob. Agents Chemother. **43**, 1317 (1999).

[7] I. Kowalski, Y. Kaconis, J. Andrae, I. Razquin-Olazaran, T. Gutsmann, G. M. de Tejada, and K. Brandenburg, Protein Pept. Lett. **17**, 1328 (2010).

[8] T. Gutsmann, I. Razquin-Olazaran, I. Kowalski, Y. Kaconis, J. Howe, R. Bartels, M. Hornef, T. Schurholz, M. Rossle, S. Sanchez-Gomez, I. Moriyon, G. M. de Tejada, and K. Brandenburg, Antimicrob. Agents Chemother. **54**, 3817 (2010).

[9] K. Brandenburg, J. Andra, P. Garidel, and T. Gutsmann, Appl. Microbiol. Biotechnol. **90**, 799 (2011).

[10] L. P. Kotra, D. Golemi, N. A. Amro, G. Y. Liu, and S. Mobashery, J. Am. Chem. Soc. **121**, 8707 (1999).

[11] R. D. Lins and T. P. Straatsma, Biophys. J **81**, 1037 (2001).

[12] R. M. Shroll and T. P. Straatsma, Biopolymers **65**, 395 (2002).

[13] D. A. Pink, L. T. Hansen, T. A. Gill, B. E. Quinn, M. H. Jericho, and T. J. Beveridge, Langmuir **19**, 8852 (2003).

[14] R. G. Oliveira, E. Schneck, B. E. Quinn, O. V. Konovalov, K. Brandenburg, T. Gutsmann, T. Gill, C. B. Hanna, D. A. Pink, and M. Tanaka, Phys. Rev. E **81**, 041901 (2010).

[15] R. G. Oliveira, E. Schneck, B. E. Quinn, O. V. Konovalov, K. Brandenburg, U. Seydel, T. Gill, C. B. Hanna, D. A. Pink, and M. Tanaka, C. R. Chim. **12**, 209 (2009).

[16] E. Schneck, E. Papp-Szabo, B. E. Quinn, O. V. Konovalov, T. J. Beveridge, D. A. Pink, and M. Tanaka, J. R. Soc., Interface **6**, S671 (2009).

[17] E. Schneck, T. Schubert, O. V. Konovalov, B. E. Quinn, T. Gutsmann, K. Brandenburg, R. G. Oliveira, D. A. Pink, and M. Tanaka, Proc. Natl. Acad. Sci. U.S.A. **107**, 9147 (2010).

[18] B. H. Jiao, M. Freudenberg, and C. Galanos, Eur. J. Biochem. **180**, 515 (1989).

[19] See Supplemental Material at http://link.aps.org/supplemental/10.1103/PhysRevE.88.012705 for chemical structure of LPS RA, pressure-area isotherms, the background subtraction, fluorescence intensities from chloride, z resolution of GIXF, error bars of XRR, and XRR of LPS Ra and P19.

[20] K. Brandenburg and U. Seydel, Biochim. Biophys. Acta, Biomembr. **775**, 225 (1984).

[21] T. Abraham, S. R. Schooling, T. J. Beveridge, and J. Katsaras, Biomacromolecules **9**, 2799 (2008).

[22] T. A. Gill, D. S. Singer, and J. W. Thompson, Process Biochem. **41**, 1875 (2006).

[23] L. G. Parratt, Phys. Rev. **95**, 359 (1954).

[24] T. Metin, in *X-Ray Scattering from Soft-Matter Thin Films* (Springer, Berlin, Heidelberg, 1999), p. 5.

[25] A. Nelson, J. Appl. Crystallogr. **39**, 273 (2006).

[26] J. Als-Nielsen and D. McMorrow, in *Elements of Modern X-ray Physics* (John Wiley & Sons, Inc., Chichester, UK, 2011), p. 69.

[27] W. B. Yun and J. M. Bloch, J. Appl. Phys. **68**, 1421 (1990).

[28] N. N. Novikova, E. A. Yurieva, S. I. Zheludeva, M. V. Kovalchuk, N. D. Stepina, A. L. Tolstikhina, R. V. Gaynutdinov, D. V. Urusova, T. A. Matkovskaya, A. M. Rubtsov, O. D. Lopina, A. I. Erko, and O. V. Konovalov, J. Synchrotron Radiat. **12**, 511 (2005).

[29] K. Ohta and H. Ishida, Appl. Opt. **29**, 1952 (1990).

[30] R. M. A. Azzam and N. M. Bashara, *Ellipsometry and Polarized Light* (North-Holland, Amsterdam, 1977).

[31] J. Daillant and A. Gibaud, in *X-ray and Neutron Reflectivity: Principles and Applications* (Springer, Berlin, Heidelberg, 1999), p. 87.

[32] P. T. Boggs, J. R. Donaldson, R. H. Byrd, and R. B. Schnabel, ACM Trans. Math. Software **15**, 348 (1989).

[33] J. Daillant, L. Bosio, J. J. Benattar, and C. Blot, Langmuir **7**, 611 (1991).

[34] C. A. Helm, L. A. Laxhuber, H. Mohwald, K. Kjaer, and J. Alsnielsen, Biophys. J. **51**, A205 (1987).

[35] K. Kjaer, J. Alsnielsen, C. A. Helm, P. Tippmankrayer, and H. Mohwald, J. Phys. Chem. **93**, 3200 (1989).

[36] M. Weygand, B. Wetzer, D. Pum, U. B. Sleytr, N. Cuvillier, K. Kjaer, P. B. Howes, and M. Losche, Biophys. J. **76**, 458 (1999).

[37] J. Majewski, T. L. Kuhl, K. Kjaer, and G. S. Smith, Biophys. J. **81**, 2707 (2001).

[38] V. Padmanabhan, J. Daillant, L. Belloni, S. Mora, M. Alba, and O. Konovalov, Phys. Rev. Lett. **99**, 086105 (2007).

[39] B. W. Matthews, J. Mol. Biol. **33**, 491 (1968).

[40] Y. Harpaz, M. Gerstein, and C. Chothia, Structure **2**, 641 (1994).

[41] Y. Kaconis, I. Kowalski, J. Howe, A. Brauser, W. Richter, I. Razquin-Olazaran, M. Inigo-Pestana, P. Garidel, M. Rossle, G. M. de Tejada, T. Gutsmann, and K. Brandenburg, Biophys. J. **100**, 2652 (2011).

[42] R. Potter, L. T. Hansen, and T. A. Gill, Int. J. Food Microbiol. **103**, 23 (2005).

[43] Y. Levin, A. P. dos Santos, and A. Diehl, Phys. Rev. Lett. **103**, 257802 (2009).

[44] A. P. dos Santos, A. Diehl, and Y. Levin, Langmuir **26**, 10778 (2010).

[45] A. P. dos Santos, A. Bakhshandeh, and Y. Levin, J. Chem. Phys. **135**, 044124 (2011).

[46] A. P. dos Santos, A. Diehl, and Y. Levin, J. Chem. Phys. **132**, 104105 (2010).